

Interpretable Deep Neural Network for Modeling Functional Surrogates

Yeseul Jeon Rajarshi Guhaniyogi Aaron Scheffler Devin Francom
Donatella Pasqualini

Abstract

Developing surrogates for computer models has become increasingly important for addressing complex problems in science and engineering. This article introduces an artificial intelligent (AI) surrogate, referred to as the *DeepSurrogate*, for analyzing functional outputs with vector-valued inputs. The relationship between the functional output and vector-valued input is modeled as an infinite sequence of unknown functions, each representing the relationship at a specific location within the functional domain. These spatially indexed functions are expressed through a combination of basis functions and their corresponding coefficient functions, both of which are modeled using deep neural networks (DNN). The proposed framework accounts for spatial dependencies across locations, while capturing the relationship between the functional output and scalar predictors. It also integrates a Monte Carlo (MC) dropout strategy to quantify prediction uncertainty, enhancing explainability in the deep neural network architecture. The proposed method enables efficient inference on datasets with approximately 50,000 spatial locations and 20 simulations, achieving results in under 10 minutes using standard hardware. The approach is validated on extensive synthetic datasets and a large-scale simulation from the Sea Lake and Overland Surge from Hurricanes (SLOSH) simulator. An open-source Python package implementing the method is made available.

Keywords: Deep neural network; functional data; large scale simulations; Monte Carlo dropout; uncertainty quantification.

1 Introduction

Scientific analysis in environmental applications often relies on simulations from computer models generating high-resolution functional data, such as climate and weather systems [Petersen et al.,

2019, Borge et al., 2008]. These simulators face key challenges in terms of significant computational resources and run times, as well as characterizing uncertainty in input attributes for reliable conclusions [Marrel et al., 2011, El-Shaarawi and Piegorsch, 2002]. Input uncertainty can be addressed intrusively, by modifying the simulation model to propagate uncertainty [Xiu and Karniadakis, 2002, Najm, 2009], or non-intrusively, by treating the simulator as a black box and running it at various settings [Santner, 2003, Higdon et al., 2004]. Non-intrusive methods are more practical as they avoid altering the simulator’s structure. However, this approach involves conducting numerous runs of the simulator with various input settings, and each of these runs comes with substantial computational costs for complex simulators. As a result, the process of simulating multiple runs is significantly expensive for many simulators and often infeasible in terms of computational resources. To mitigate this, statistical surrogates (or emulators) are often built to approximate the simulator. Once trained, these emulators enable faster predictions, facilitating studies of model response and parameter uncertainty.

This manuscript is motivated by physics-based simulations that use a hurricane’s track and hurricane-related attributes as inputs to generate output of a function of storm surge over a large spatial grid, or flood depth measurements above normal levels (e.g., water depth above ground at land locations). The primary goal is to model the maximum flood depth across the entire spatial domain as a functional output, enabling predictive inference of this function for untested hurricane tracks and attributes, quantifying uncertainty, and achieving these results significantly faster than actually running such physics-based simulations for a large number for uncertainty quantification (UQ).

The scientific problem can be formulated within a function-on-scalar (FoS) regression framework, where much of the existing literature emphasizes functional linear models (FLM). In these models, functionally varying coefficients corresponding to scalar predictors are employed to capture and explain variations in a functional response. Early approaches to FoS regression primarily relied on basis function expansions, where both the response and coefficient functions are expressed using a finite set of basis functions [Reiss and Ogden, 2007]. This transformation reduces the infinite-dimensional problem into a manageable finite-dimensional one, enabling the use of standard regression techniques to estimate the coefficients effectively. Another widely adopted method is penalized functional regression, which incorporates smoothness penalties (e.g., roughness penal-

ties on derivatives of coefficient functions) during estimation [Goldsmith et al., 2011]. Additionally, functional principal component regression (FPCR) has been employed to reduce the dimensionality of functional responses [Yao and Lee, 2006, Goldsmith et al., 2015]. In FPCR, principal components of the functional responses are extracted, and regression is performed on these reduced components, preserving essential information while reducing computational complexity. Beyond the FLM framework, several nonlinear approaches have been developed to address more intricate regression scenarios. For example, Zhang and Wang [2015] combined the FoS regression framework with additive models, removing the linearity assumption between scalar predictors and the functional response. This enhancement provides greater flexibility in modeling complex relationships. Expanding on this idea, Scheipl et al. [2015] proposed the functional additive mixed (FAM) model, offering a more generalized extension of the additive approach.

However, these traditional methods are not designed to explicitly quantify uncertainty in predictions of functional outcomes. To address this limitation, Bayesian approaches have gained traction in the FoS regression framework [Morris, 2015]. A class of Bayesian approaches employs varying coefficient models, with varying coefficients capturing the complex non-linear association between functional outcome and scalar response [Andros et al., 2024]. Although Gaussian Process (GP) priors are an attractive choice for varying coefficients due to their flexibility, smooth interpolation capabilities, and built-in uncertainty quantification for predictive distributions [Santner, 2003, Gramacy, 2020], they suffer from significant computational limitations, primarily due to the need to invert large covariance matrices, which hampers their scalability for large datasets.

Developing surrogates with large functional data in computer experiments has garnered increasing interest, leading to a burgeoning literature on scalable methods, many of which draw from advancements in scalable spatial modeling. These approaches include multi-resolution methods [Guhaniyogi and Sanso, 2020], local Gaussian processes [Gramacy and Apley, 2015], deep Gaussian processes [Sauer et al., 2023], and robust distributed Bayesian inference [Andros et al., 2024]. Full inference typically requires efficient algorithms, such as Markov chain Monte Carlo (MCMC) [Guhaniyogi et al., 2022, 2023], variational approximations [Gal and Ghahramani, 2016], and Gaussian Markov random field approximations (Rue et al. [2009], Lindgren et al. [2011] and references therein). Beyond efficient variants of GPs, alternative Bayesian modeling of surrogates have emerged as competitive options. For instance, BASS [Francom and Sansó, 2020] employs adap-

tive splines for functional data modeling, while BART [Chipman et al., 2010] leverages additive regression trees.

Several existing works have explored the integration of deep neural networks (DNNs) into functional data analysis for rapid computation with big data, primarily in the setting where a functional input is employed in the modeling of a scalar output. For instance, Rossi et al. [2002], Rossi and Conan-Guez [2005] were among the first to introduce the concept of a functional neural network (FNN), incorporating functional neurons in the first hidden layer to process functional inputs. This approach was later extended by Thind et al. [2020, 2023], enabling FNNs to handle both functional and scalar variables as inputs while modeling a scalar output. Rao et al. [2020] further enhanced FNNs by incorporating geographically weighted regression and spatial autoregressive techniques to address regression problems involving spatially correlated functional data. Additionally, Wang et al. [2020] proposed a nonlinear function-on-function regression model using a fully connected NN. In another advancement, Yao et al. [2021] developed a neural network with a novel basis layer, where the hidden neurons were micro NNs designed to perform parsimonious dimension reduction of functional inputs, leveraging information relevant to a scalar output. Wang and Cao [2024] introduced a functional nonlinear learning framework to effectively represent multivariate functional data in a reduced-dimensional feature space. Meanwhile, Wang and Cao [2023] proposed a nonlinear prediction methodology tailored for functional time series.

1.1 Proposed Model and Novelty of the Contribution

Most of the aforementioned works are focused on building NNs with functional inputs and scalar outputs. In contrast, this article focuses on capturing complex non-linear relationship between functional output with vector-valued inputs using the deep learning architecture. To elaborate on it, we express the relationship between the functional output and vector input using an infinite sequence of spatially-indexed regression functions, where a representative regression function captures association between the output and vector inputs at a location in the domain. To account for spatial association between these unknown regression functions, we assume a basis representation with basis functions capturing the non-linear effect of inputs and spatially-indexed basis coefficient functions account for spatial association between regression functions at different locations. Deep neural network with a dropout architecture is employed to model both basis functions and basis

coefficient functions. We implement *MC dropout*, exploiting the connection between deep GP and deep neural network with dropout, to draw point prediction, as well as uncertainty quantification in prediction of the functional output.

Novelty of the proposed approach. Three main contributions are made in this paper. (1)

Data driven basis function estimation. A considerable body of literature on functional data models assumes fixed basis functions (e.g., B-spline, wavelet basis) and focuses primarily on modeling the basis coefficients. In contrast, the proposed approach introduces flexible modeling of both the basis functions and the basis coefficient functions through separate deep neural network (DNN) architectures, offering several key advantages. First, the data-driven estimation of basis functions using DNNs adapts seamlessly to spatial variations in complex data structures via non-linear activation functions. This flexibility is challenging to achieve with pre-fixed bases, which require explicit modifications to handle such variations, often adding complexity. Second, DNNs are inherently optimized to enhance predictive performance and are versatile, enabling them to generalize across a broad range of functional data types and domains. Unlike fixed basis functions, which necessitate extensive manual adjustments, DNN-based modeling provides a highly efficient, task-specific representation, streamlining the modeling process and improving adaptability. (2)

Scalability. Our framework is highly scalable, completing analysis for 20 simulations and approximately 50,000 spatial locations per simulation within 10 minutes, demonstrating its suitability for large-scale simulations. Its computation time is comparable with state-of-the-art scalable GP methods for FoS regression, while providing significantly improved uncertainty quantification, as demonstrated through empirical evaluations. (3) **Explainable deep neural network architecture.** Our approach leverages the connection between deep Gaussian processes and deep neural networks (DNN) with dropout architecture to quantify uncertainty in predictions. Beyond this, it enables inference on the sequence of spatially-indexed functions that encapsulate the relationship between functional outcomes and vector-valued inputs. This enhances the interpretability of the model, contributing to the growing field of explainable AI systems for functional data. Recently, Wu et al. [2023] introduced a deep neural network approach for FoS regression. In their method, the functional outcome is first represented in a lower-dimensional space using either a basis expansion strategy or functional principal components. The resulting basis coefficients or principal component scores are then modeled using a deep neural network with scalar inputs. While this approach

effectively provides point predictions for the functional outcome, it does not offer a mechanism for quantifying uncertainty in the inference. To the best of our knowledge, our proposed method represents the first explainable AI framework specifically designed for modeling functional surrogates of computer models, bridging the gap between predictive accuracy, scalability and interpretability.

2 Model Development

Let $\mathbf{z}_h = (z_{h,1}, \dots, z_{h,p})^T$ represent the p -dimensional input for the h -th simulation, which generates a functional output $(y_h(\mathbf{s}) : \mathbf{s} \in \mathcal{S})^T$, where $\mathcal{S} \subseteq \mathbb{R}^2$ denotes a compact domain. Additionally, assume that each functional outcome is influenced at each location \mathbf{s} by a vector of covariates $\mathbf{x}(\mathbf{s}) = (x_1(\mathbf{s}), \dots, x_q(\mathbf{s}))^T$, which is common to all simulations and referred to as *fine-scale covariates*. Our focus is on modeling the nonlinear relationship between the vector-valued input and the functional outcome, while accounting for the effects of the fine-scale covariates.

We capture the effects of vector input using a semi-parametric additive regression framework, expressed as,

$$y_h(\mathbf{s}) = \beta_0 + \mathbf{x}(\mathbf{s})^T \boldsymbol{\beta} + f_{\mathbf{s}}(\mathbf{z}_h) + \epsilon_h(\mathbf{s}), \quad \mathbf{s} \in \mathcal{S}, \quad h = 1, \dots, H, \quad (1)$$

where $\beta_0 \in \mathbb{R}$ is the intercept, $\boldsymbol{\beta} \in \mathbb{R}^q$ is the coefficient vector capturing the effect of fine-scale covariates, and $f_{\mathbf{s}}(\cdot)$ captures the nonlinear influence of the vector-valued input at location \mathbf{s} . The idiosyncratic errors are assumed to follow $\epsilon_h(\mathbf{s}) \stackrel{i.i.d.}{\sim} N(0, \delta^2)$. While this model assumes Gaussian functional outcomes, it can be readily extended to accommodate scenarios where $y_h(\mathbf{s})$ is binary, categorical or count-valued.

Let $\mathcal{F}(\mathcal{S}) = \{f_{\mathbf{s}}(\cdot) : \mathbf{s} \in \mathcal{S}\}$ denote the uncountable set of functions, where each function characterizes the effect of inputs at a specific spatial location. Our goal is to jointly model the functions in $\mathcal{F}(\mathcal{S})$ while enabling spatial information sharing. Specifically, for locations \mathbf{s} and \mathbf{s}' that are close to each other in \mathcal{S} , we aim to facilitate greater information sharing in the estimation of $f_{\mathbf{s}}(\cdot)$ and $f_{\mathbf{s}'}(\cdot)$. To achieve this with added flexibility, each function $f_{\mathbf{s}}(\cdot)$ is modeled with a linear combination of K basis functions $B_1(\mathbf{z}_h), \dots, B_K(\mathbf{z}_h)$ with their corresponding spatially-varying

coefficient functions $\eta_1(\mathbf{s}), \dots, \eta_K(\mathbf{s})$, respectively, given by,

$$f_{\mathbf{s}}(\mathbf{z}_h) = \sum_{k=1}^K B_k(\mathbf{z}_h) \eta_k(\mathbf{s}) = \boldsymbol{\eta}(\mathbf{s})^T \mathbf{B}(\mathbf{z}_h), \quad \mathbf{s} \in \mathcal{S}, \quad h = 1, \dots, H, \quad (2)$$

where $\boldsymbol{\eta}(\mathbf{s}) = (\eta_1(\mathbf{s}), \dots, \eta_K(\mathbf{s}))^T$ is the vector of basis coefficient function at location \mathbf{s} and $\mathbf{B}(\mathbf{z}_h) = (B_1(\mathbf{z}_h), \dots, B_K(\mathbf{z}_h))^T$ is the vector of basis functions evaluated at \mathbf{z}_h .

A substantial body of existing literature assumes pre-specified basis functions, with B-spline bases being the most widely used due to their attractive theoretical properties [Guhaniyogi et al., 2024]. Other commonly used options include wavelet bases [Vidakovic, 2009, Cressie, 2015], radial basis functions [Bliznyuk et al., 2008], and locally bi-square [Cressie and Johannesson, 2008]. However, these pre-defined basis functions often demand substantial manual adjustments to accommodate complex functional data types and domains, especially when addressing nonlinearity in regression [Gomes and Senne, 2014, Zhang and Dower, 2013]. To overcome these limitations, this article treats both basis functions and basis coefficient functions as unknown and estimates them using deep neural network architectures, providing significantly enhanced flexibility. Details of this approach are outlined in the following section.

2.1 Deep Neural Network Architecture for Unknown Functions

We consider a deep neural network architecture with L_B layers, with the l_B th layer having $k_{l_B}^{(B)}$ nodes ($l_B = 1, \dots, L_B$), to model the unknown K -dimensional vector of basis functions $\mathbf{B}(\mathbf{z}) \in \mathbb{R}^K$ evaluated at an input \mathbf{z} , given by

$$\mathbf{B}(\mathbf{z}) = \sigma_{L_B}^{(B)} \left(\mathbf{W}_{L_B}^{(B)} \sigma_{L_{B-1}}^{(B)} \left(\dots \sigma_2^{(B)} \left(\mathbf{W}_2^{(B)} \sigma_1^{(B)} \left(\mathbf{W}_1^{(B)} \mathbf{z} + \mathbf{b}_1^{(B)} \right) + \mathbf{b}_2^{(B)} \right) \dots \right) + \mathbf{b}_{L_B}^{(B)} \right). \quad (3)$$

The weight matrix $\mathbf{W}_{l_B}^{(B)} \in \mathbb{R}^{k_{l_B}^{(B)} \times k_{l_{B-1}}^{(B)}}$ connects the $(l_B - 1)$ th layer to the l_B th hidden layer, $\sigma_{l_B}^{(B)}$ is the activation function for the l_B th layer, and $\mathbf{b}_{l_B}^{(B)} \in \mathbb{R}^{k_{l_B}^{(B)}}$ represents the bias parameter.

Similarly, we adopt a DNN architecture with L_η layers to model the vector of basis coefficient functions, $\boldsymbol{\eta}(\mathbf{s}) \in \mathbb{R}^K$. With the l_η th layer containing $k_{l_\eta}^{(\eta)}$ nodes, the architecture is specified as,

$$\boldsymbol{\eta}(\mathbf{s}) = \sigma_{L_\eta}^{(\eta)} \left(\mathbf{W}_{L_\eta}^{(\eta)} \sigma_{L_\eta-1}^{(\eta)} \left(\dots \sigma_2^{(\eta)} \left(\mathbf{W}_2^{(\eta)} \sigma_1^{(\eta)} \left(\mathbf{W}_1^{(\eta)} \mathbf{s} + \mathbf{b}_1^{(\eta)} \right) + \mathbf{b}_2^{(\eta)} \right) \dots \right) + \mathbf{b}_{L_\eta}^{(\eta)} \right). \quad (4)$$

Here $\mathbf{W}_{l_\eta}^{(\eta)} \in \mathbb{R}^{k_{l_\eta}^{(\eta)} \times k_{l_\eta-1}^{(\eta)}}$ is the weight matrix, $\sigma_{l_\eta}^{(\eta)}$ is the activation function for the l_η th layer, and $\mathbf{b}_{l_\eta}^{(\eta)} \in \mathbb{R}^{k_{l_\eta}^{(\eta)}}$ represents the bias parameter, $l_\eta = 1, \dots, L_\eta$. The DNN architecture in (3) enables borrowing of information across the input space, while the DNN architecture in (4) facilitates information sharing between functions in $\mathcal{F}(\mathcal{S})$ across the spatial domain \mathcal{S} . By training basis function $\mathbf{B}(\mathbf{z})$ and the basis coefficient functions $\eta(\mathbf{s})$ across different layers in DNN, as shown in (3) and (4), our model combine them in the final layer of the DNN, along with the local covariate, to construct the model in (1). Figure 1 illustrates the training mechanism for the proposed AI-driven surrogate model.

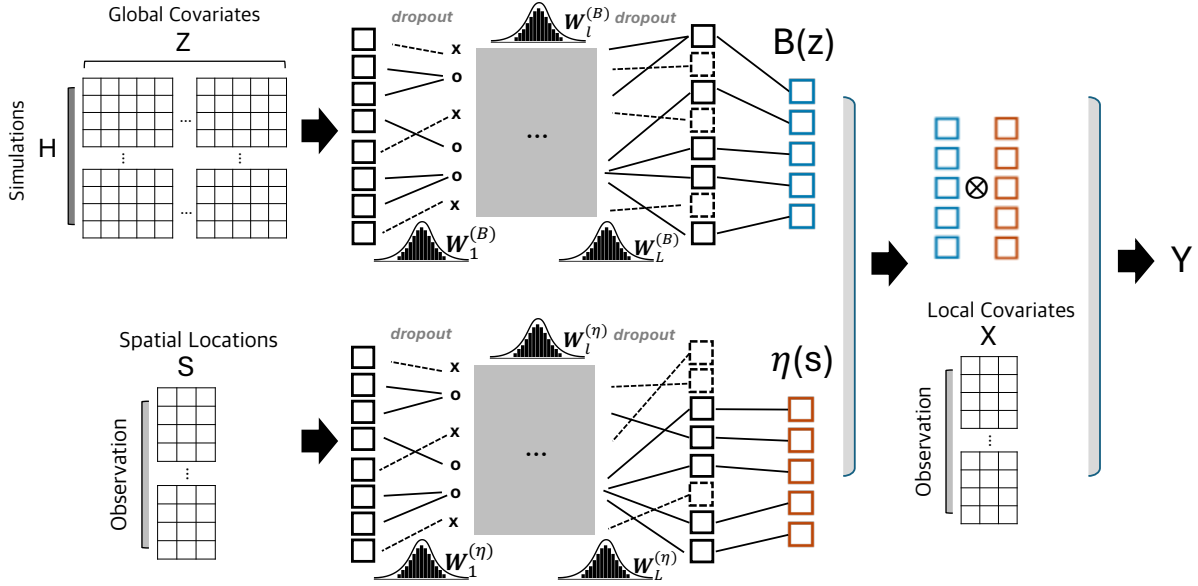


Figure 1: A graphical illustration of AI-driven surrogate model

With data observed at locations $\mathbf{s}_1, \dots, \mathbf{s}_n$ for each of the H simulations, a traditional deep neural network approach proceeds to train the model by minimizing the following loss function,

$$\begin{aligned} \mathcal{L}_{\text{DNN}}(\beta_0, \boldsymbol{\beta}, \delta^2, \boldsymbol{\theta}) := & \frac{1}{2nH} \sum_{i=1}^n \sum_{h=1}^H \frac{(y_h(\mathbf{s}_i) - \hat{y}_h(\mathbf{s}_i))^2}{\delta^2} + \sum_{l_B=1}^{L_B} \lambda_{l_B}^{(W)} \left\| \mathbf{W}_{l_B}^{(B)} \right\|_2^2 + \sum_{l_B=1}^{L_B} \lambda_{l_B}^{(b)} \left\| \mathbf{b}_{l_B}^{(B)} \right\|_2^2, \\ & + \sum_{l_\eta=1}^{L_\eta} \lambda_{l_\eta}^{(W)} \left\| \mathbf{W}_{l_\eta}^{(\eta)} \right\|_2^2 + \sum_{l_\eta=1}^{L_\eta} \lambda_{l_\eta}^{(b)} \left\| \mathbf{b}_{l_\eta}^{(\eta)} \right\|_2^2 \end{aligned} \quad (5)$$

where $\| \cdot \|_2$ denotes the l_2 norm, $\hat{y}_h(\mathbf{s}_i) = \beta_0 + \mathbf{x}(\mathbf{s}_i)' \boldsymbol{\beta} + \boldsymbol{\eta}(\mathbf{s}_i)' \mathbf{B}(\mathbf{z}_h)$, and $\lambda_{l_B}^{(W)}, \lambda_{l_B}^{(b)}, \lambda_{l_\eta}^{(W)}, \lambda_{l_\eta}^{(b)}$

are penalty parameters controlling shrinkage for weight and bias parameters. The set of unknown parameters $\theta = \{(\mathbf{W}_{l_B}^{(B)}, \mathbf{b}_{l_B}^{(B)}), l_B = 1, \dots, L_B\} \cup \{(\mathbf{W}_{l_\eta}^{(\eta)}, \mathbf{b}_{l_\eta}^{(\eta)}), l_\eta = 1, \dots, L_\eta\}$ belong to the parameter space Θ . By imposing regularization on the connections between layers, known as the *dropout architecture*, the proposed framework prevent overfitting. The aforementioned DNN framework cannot quantify uncertainties, which is central to the predictive inference from statistical emulators. To address this limitation, we leverage the connection between deep Gaussian processes and deep neural networks with dropout imposed on every layer, following Gal and Ghahramani [2016]. The deep Gaussian process architecture enables uncertainty quantification (UQ) in inference and prediction within the proposed framework, as discussed below.

3 Inference

3.1 A Bayesian Deep Neural Network: A Deep Gaussian Process Approximation

The work of Gal and Ghahramani [2016] demonstrated that a neural network of arbitrary depth and non-linearities, when applying dropout before each deep layer, is equivalent to an approximation of a probabilistic deep Gaussian Process [Damianou and Lawrence, 2013] marginalized over its covariance function. Specifically, the dropout architecture effectively minimizes the Kullback–Leibler (KL) divergence between an approximate distribution and the posterior of a deep Gaussian process, marginalized over its finite-rank covariance function parameters. Additionally, it has been emphasized that no simplifying assumptions were made regarding the use of dropout in the literature. As a result, the derived findings apply broadly to any neural network architecture that incorporates dropout.

Define a sequence of random linear features $\{\mathbf{f}_{h,l_B}^{(B)} \in \mathbb{R}^{k_{l_B}^{(B)}} : l_B = 1, \dots, L_B; h = 1, \dots, H\}$ over L_B layers, with the features in the l_B th layer are of dimensions $k_{l_B}^{(B)}$. Let $\mathbf{F}_{l_B}^{(B)} = [\mathbf{f}_{1,l_B}^{(B)} : \dots : \mathbf{f}_{H,l_B}^{(B)}]^T \in \mathbb{R}^{H \times k_{l_B}^{(B)}}$ be a matrix formed by stacking features in the l_B th layer, with the k th column of $\mathbf{F}_{l_B}^{(B)}$ is given by $\mathbf{f}_{l_B}^{(k)(B)}$, ($k = 1, \dots, k_{l_B}^{(B)}$). Similarly, define a sequence of random linear features $\{\mathbf{f}_{i,l_\eta}^{(\eta)} \in \mathbb{R}^{k_{l_\eta}^{(\eta)}} : l_\eta = 1, \dots, L_\eta; i = 1, \dots, n\}$ and construct the matrix $\mathbf{F}_{l_\eta}^{(\eta)} = [\mathbf{f}_{1,l_\eta}^{(\eta)} : \dots : \mathbf{f}_{n,l_\eta}^{(\eta)}]^T \in \mathbb{R}^{n \times k_{l_\eta}^{(\eta)}}$ by stacking features in the l_η th layer. Let the k th column of $\mathbf{F}_{l_\eta}^{(\eta)}$ be given by $\mathbf{f}_{l_\eta}^{(k)(\eta)}$, ($k = 1, \dots, k_{l_\eta}^{(\eta)}$). Assuming independence between columns of $\mathbf{F}_{l_B}^{(B)}$ given $\mathbf{F}_{l_{B-1}}^{(B)}$, and independence between columns of $\mathbf{F}_{l_\eta}^{(\eta)}$ given $\mathbf{F}_{l_{\eta-1}}^{(\eta)}$, we construct two deep Gaussian processes with L_B and L_η layers as a generative

models for $\mathbf{B}(\mathbf{z}_h)$ and $\boldsymbol{\eta}(\mathbf{s}_i)$, respectively. Conditional on the previous layer, the finite dimensional realization of the deep GP for the two generative models are given by,

$$\begin{aligned}\mathbf{f}_{l_B}^{(k)(B)} | \mathbf{F}_{l_{B-1}}^{(B)}, \mathbf{W}_{l_B}^{(B)}, \mathbf{b}_{l_B}^{(B)} &\sim N(\mathbf{0}, \boldsymbol{\Sigma}_{l_B}^{(B)}), \quad l_B = 2, \dots, L_B \\ \mathbf{f}_{l_\eta}^{(k)(\eta)} | \mathbf{F}_{l_{\eta-1}}^{(\eta)}, \mathbf{W}_{l_\eta}^{(\eta)}, \mathbf{b}_{l_\eta}^{(\eta)} &\sim N(\mathbf{0}, \boldsymbol{\Sigma}_{l_\eta}^{(\eta)}), \quad l_\eta = 2, \dots, L_\eta,\end{aligned}\tag{6}$$

where the covariance matrices $\boldsymbol{\Sigma}_{l_B}^{(B)} \in \mathbb{R}^{H \times H}$, $\boldsymbol{\Sigma}_{l_\eta}^{(\eta)} \in \mathbb{R}^{n \times n}$ for the finite dimensional realizations depend on the previous layer. Specifically,

$$\begin{aligned}\boldsymbol{\Sigma}_{l_B}^{(B)} &= \int \sigma_{l_B}^{(B)}(\boldsymbol{\Phi}_{l_{B-1}}^{(B)} \mathbf{w}^{(B)} + \mathbf{b}^{(B)}) \sigma_{l_B}^{(B)}(\boldsymbol{\Phi}_{l_{B-1}}^{(B)} \mathbf{w}^{(B)} + \mathbf{b}^{(B)})^\top p(\mathbf{w}^{(B)}) p(\mathbf{b}^{(B)}), \\ \boldsymbol{\Sigma}_{l_\eta}^{(\eta)} &= \int \sigma_{l_\eta}^{(\eta)}(\boldsymbol{\Phi}_{l_{\eta-1}}^{(\eta)} \mathbf{w}^{(\eta)} + \mathbf{b}^{(\eta)}) \sigma_{l_\eta}^{(\eta)}(\boldsymbol{\Phi}_{l_{\eta-1}}^{(\eta)} \mathbf{w}^{(\eta)} + \mathbf{b}^{(\eta)})^\top p(\mathbf{w}^{(\eta)}) p(\mathbf{b}^{(\eta)}),\end{aligned}\tag{7}$$

where $\boldsymbol{\Phi}_{l_B}^{(B)} = [\phi_{1,l_B}^{(B)} : \dots : \phi_{H,l_B}^{(B)}]^\top \in \mathbb{R}^{H \times k_{l_B}^{(B)}}$ are the collection of feature vectors after applying the activation function, such that $\phi_{h,l_B}^{(B)} = \sigma_{l_B}^{(B)}(\mathbf{f}_{h,l_B}^{(B)})$. Similarly, $\boldsymbol{\Phi}_{l_\eta}^{(\eta)} = [\phi_{1,l_\eta}^{(\eta)} : \dots : \phi_{n,l_\eta}^{(\eta)}]^\top \in \mathbb{R}^{n \times k_{l_\eta}^{(\eta)}}$ are the collection of feature vectors after transformation such that $\phi_{i,l_\eta}^{(\eta)} = \sigma_{l_\eta}^{(\eta)}(\mathbf{f}_{i,l_\eta}^{(\eta)})$.

We approximate $\boldsymbol{\Sigma}_{l_B}^{(B)}$ through Monte Carlo integration over $k_{l_B}^{(B)}$ columns of $\mathbf{W}_{l_B}^{(B)}$ at the l_B th layer, and approximate $\boldsymbol{\Sigma}_{l_\eta}^{(\eta)}$ through Monte Carlo integration over $k_{l_\eta}^{(\eta)}$ columns of $\mathbf{W}_{l_\eta}^{(\eta)}$, leading to

$$\begin{aligned}\widehat{\boldsymbol{\Sigma}}_{l_B}^{(B)} &= \frac{1}{k_{l_B}^{(B)}} \sigma_{l_B}^{(B)}(\boldsymbol{\Phi}_{l_{B-1}}^{(B)} \mathbf{W}_{l_B}^{\top(B)} + \mathbf{b}_{l_B}^{(B)}) \sigma_{l_B}^{(B)}(\boldsymbol{\Phi}_{l_{B-1}}^{(B)} \mathbf{W}_{l_B}^{\top(B)} + \mathbf{b}_{l_B}^{(B)})^\top \\ \widehat{\boldsymbol{\Sigma}}_{l_\eta}^{(\eta)} &= \frac{1}{k_{l_\eta}^{(\eta)}} \sigma_{l_\eta}^{(\eta)}(\boldsymbol{\Phi}_{l_{\eta-1}}^{(\eta)} \mathbf{W}_{l_\eta}^{\top(\eta)} + \mathbf{b}_{l_\eta}^{(\eta)}) \sigma_{l_\eta}^{(\eta)}(\boldsymbol{\Phi}_{l_{\eta-1}}^{(\eta)} \mathbf{W}_{l_\eta}^{\top(\eta)} + \mathbf{b}_{l_\eta}^{(\eta)})^\top,\end{aligned}\tag{8}$$

According to Gal and Ghahramani [2016], (8) becomes accurate in approximating the true covariance matrix as $k_{l_B}^{(B)}$ and $k_{l_\eta}^{(\eta)}$ increase.

Assuming that the final layer in both generative models consists of K components, i.e., $k_{L_B}^{(B)} = k_{L_\eta}^{(\eta)} = K$, we estimate the basis functions and basis coefficients using the features from this last layer. Specifically, we set $\mathbf{B}(\mathbf{z}_h) = \mathbf{f}_{h,L_B}^{(B)}$ ($i = 1, \dots, n$) and $\boldsymbol{\eta}(\mathbf{s}_i) = \mathbf{f}_{i,L_\eta}^{(\eta)}$ ($i = 1, \dots, n$). The

generative AI for the functional surrogate is given by,

$$\begin{aligned}
y_h(\mathbf{s}_i) | \mathbf{F}_{L_B}^{(B)}, \mathbf{F}_{L_\eta}^{(\eta)}, \mathbf{x}(\mathbf{s}_i) &\sim N(y_h(\mathbf{s}_i) | \beta_0 + \mathbf{x}(\mathbf{s}_i)^T \boldsymbol{\beta} + \mathbf{B}(\mathbf{z}_h)^T \boldsymbol{\eta}(\mathbf{s}_i), \delta^2), \quad \mathbf{B}(\mathbf{z}_h) = \mathbf{f}_{h, L_B}^{(B)}, \quad \boldsymbol{\eta}(\mathbf{s}_i) = \mathbf{f}_{i, L_\eta}^{(\eta)} \\
\mathbf{f}_{l_B}^{(k)(B)} | \mathbf{F}_{l_{B-1}}^{(B)}, \mathbf{W}_{l_B}^{(B)}, \mathbf{b}_{l_B}^{(B)} &\sim N(\mathbf{0}, \boldsymbol{\Sigma}_{l_B}^{(B)}), \quad l_B = 2, \dots, L_B; \quad k = 1, \dots, k_{l_B}^{(B)} \\
\mathbf{f}_{l_\eta}^{(k)(\eta)} | \mathbf{F}_{l_{\eta-1}}^{(\eta)}, \mathbf{W}_{l_\eta}^{(\eta)}, \mathbf{b}_{l_\eta}^{(\eta)} &\sim N(\mathbf{0}, \boldsymbol{\Sigma}_{l_\eta}^{(\eta)}), \quad l_\eta = 2, \dots, L_\eta; \quad k = 1, \dots, k_{l_\eta}^{(\eta)}. \tag{9}
\end{aligned}$$

Since performing Bayesian inference for deep Gaussian processes (GPs) using Markov chain Monte Carlo (MCMC) is not straightforward, we adopt variational Bayesian inference known as MC dropout [Gal and Ghahramani, 2016], which is designed for deep GPs based on Monte Carlo approximation. This approach utilizes a normal mixture distribution as the variational distribution to approximate the posterior distribution. Following Gal and Ghahramani [2016], we construct a variational approximation of the posterior distribution of the parameters, enabling an approximation of the deep GP. Specifically, we define the variational distribution as $\prod_{l_B=1}^{L_B} q(\mathbf{W}_{l_B}^{(B)})q(\mathbf{b}_{l_B}^{(B)}) \prod_{l_\eta=1}^{L_\eta} q(\mathbf{W}_{l_\eta}^{(\eta)})q(\mathbf{b}_{l_\eta}^{(\eta)})$ where each term represents the variational distribution of the corresponding weight matrices and bias vectors, given by,

$$\begin{aligned}
q(\mathbf{W}_{l_B}^{(B)}) &= \prod_{\forall k, k'} q(w_{l_B, kk'}^{(B)}), \quad q(\mathbf{b}_{l_B}^{(B)}) = \prod_{\forall k} q(b_{l_B, k}^{(B)}), \quad q(\mathbf{W}_{l_\eta}^{(\eta)}) = \prod_{\forall k, k'} q(w_{l_\eta, kk'}^{(\eta)}), \quad q(\mathbf{b}_{l_\eta}^{(\eta)}) = \prod_{\forall k} q(b_{l_\eta, k}^{(\eta)}), \\
q(w_{l_B, kk'}^{(B)}) &= p_{l_B} N(\mu_{l_B, kk'}^{w(B)}, \sigma^2) + (1 - p_{l_B}) N(0, \sigma^2), \quad q(w_{l_\eta, kk'}^{(\eta)}) = p_{l_\eta} N(\mu_{l_\eta, kk'}^{w(\eta)}, \sigma^2) + (1 - p_{l_\eta}) N(0, \sigma^2) \\
q(b_{l_B, k}^{(B)}) &= p_{l_B} N(\mu_{l_B, k}^{b(B)}, \sigma^2) + (1 - p_{l_B}) N(0, \sigma^2) \quad q(b_{l_\eta, k}^{(\eta)}) = p_{l_\eta} N(\mu_{l_\eta, k}^{b(\eta)}, \sigma^2) + (1 - p_{l_\eta}) N(0, \sigma^2), \tag{10}
\end{aligned}$$

where $w_{l_B, kk'}^{(B)}$ and $w_{l_\eta, kk'}^{(\eta)}$ are the (k, k') th element of the weight matrix $\mathbf{W}_{l_B}^{(B)} \in \mathbb{R}^{k_{l_B}^{(B)} \times k_{l_B-1}^{(B)}}$ and $\mathbf{W}_{l_\eta}^{(\eta)} \in \mathbb{R}^{k_{l_\eta}^{(\eta)} \times k_{l_\eta-1}^{(\eta)}}$, respectively. Similarly, $b_{l_B, k}^{(B)}$ and $b_{l_\eta, k}^{(\eta)}$ is the k th element of the bias vector $\mathbf{b}_{l_B}^{(B)} \in \mathbb{R}^{k_{l_B}^{(B)}}$ and $\mathbf{b}_{l_\eta}^{(\eta)} \in \mathbb{R}^{k_{l_\eta}^{(\eta)}}$, respectively. For the weight parameters, $\mu_{l_B, kk'}^{w(B)}$, $\mu_{l_\eta, kk'}^{w(\eta)}$ and σ^2 are variational parameters that control the mean and spread of the distributions, respectively. Let $\tilde{\boldsymbol{\theta}}$ denotes the collection of all variational parameters $\{\mu_{l_B, kk'}^{w(B)} : l_B = 1, \dots, L_B; k = 1, \dots, k_{l_B}^{(B)}; k' = 1, \dots, k_{l_B-1}^{(B)}\}$, $\{\mu_{l_\eta, kk'}^{w(\eta)} : l_\eta = 1, \dots, L_\eta; k = 1, \dots, k_{l_\eta}^{(\eta)}; k' = 1, \dots, k_{l_\eta-1}^{(\eta)}\}$, $\{\mu_{l_B, k}^{b(B)} : l_B = 1, \dots, L_B; k = 1, \dots, k_{l_B}^{(B)}\}$, $\{\mu_{l_\eta, k}^{b(\eta)} : l_\eta = 1, \dots, L_\eta; k = 1, \dots, k_{l_\eta}^{(\eta)}\}$. As the inclusion probabilities $p_{l_B}, p_{l_\eta} \in [0, 1]$ become close to 0, $q(w_{l_B, kk'}^{(B)})$ and $q(w_{l_\eta, kk'}^{(\eta)})$ become $N(0, \sigma^2)$, indicating that it is likely to drop the weight parameters

(i.e., $w_{l_B, k k'}^{(B)} = 0$, $w_{l_\eta, k k'}^{(\eta)} = 0$). Similarly, the variational distribution for the bias parameters are modeled with a mixture normal distribution.

We denote the variational distribution of $\boldsymbol{\theta}$ as $q(\boldsymbol{\theta}|\tilde{\boldsymbol{\theta}})$ to show its dependence on the variational parameters. While we optimize $\tilde{\boldsymbol{\theta}}$ using the procedure described below, we find the optimal values of p_{l_B} , p_{l_η} and σ^2 through a grid search. Further details on the DNN architecture including the choice of p_{l_B} , p_{l_η} and σ^2 , can be found in the Web Appendix.

The optimal variational parameters $\tilde{\boldsymbol{\theta}}$ are set by minimizing the Kullback–Leibler (KL) divergence between $q(\boldsymbol{\theta}|\tilde{\boldsymbol{\theta}})$ and $\pi(\boldsymbol{\theta}|\{\{\mathbf{s}_i, \mathbf{x}(\mathbf{s}_i), \mathbf{z}, \mathbf{y}_h(\mathbf{s}_i)\}_{i=1}^n\}_{h=1}^H)$ where minimizing the KL divergence is equivalent to maximizing $\mathbb{E}_q[\log(\pi(\boldsymbol{\theta}, \{\{\mathbf{s}_i, \mathbf{x}(\mathbf{s}_i), \mathbf{z}, \mathbf{y}_h(\mathbf{s}_i)\}_{i=1}^n\}_{h=1}^H)))] - \mathbb{E}_q[\log q(\boldsymbol{\theta}|\tilde{\boldsymbol{\theta}})]$, the evidence lower bound (ELBO). With the mean field variational distribution $q(\boldsymbol{\theta}|\tilde{\boldsymbol{\theta}})$, the log ELBO of our model is given by,

$$\begin{aligned} \mathcal{L}_{\text{GP-VI}}(\beta_0, \boldsymbol{\beta}, \delta^2, \tilde{\boldsymbol{\theta}}) &= \sum_{i=1}^n \sum_{h=1}^H \int \cdots \int q(\boldsymbol{\theta}|\tilde{\boldsymbol{\theta}}) \log p(\mathbf{y}_h(\mathbf{s}_i)|\mathbf{x}(\mathbf{s}_i), \mathbf{z}_h, \beta_0, \boldsymbol{\beta}, \delta^2, \mathbf{F}_{L_B}^{(B)}, \mathbf{F}_{L_\eta}^{(\eta)}) \\ &\quad \prod_{l_B=2}^{L_B} p(\mathbf{F}_{l_B}^{(B)}|\mathbf{F}_{l_{B-1}}^{(B)}, \mathbf{W}_{l_B}^{(B)}, \mathbf{b}_{l_B}^{(B)}) \prod_{l_\eta=2}^{L_\eta} p(\mathbf{F}_{l_\eta}^{(\eta)}|\mathbf{F}_{l_{\eta-1}}^{(\eta)}, \mathbf{W}_{l_\eta}^{(\eta)}, \mathbf{b}_{l_\eta}^{(\eta)}) d\mathbf{W}_{l_\eta}^{(\eta)} d\mathbf{b}_{l_\eta}^{(\eta)}, d\mathbf{W}_{l_B}^{(B)} d\mathbf{b}_{l_B}^{(B)} \\ &\quad - \text{KL} \left(\prod_{l_B=1}^{L_B} q(\mathbf{W}_{l_B}^{(B)}) q(\mathbf{b}_{l_B}^{(B)}) \prod_{l_\eta=1}^{L_\eta} q(\mathbf{W}_{l_\eta}^{(\eta)}) q(\mathbf{b}_{l_\eta}^{(\eta)}) \middle| \middle| p(\{\{\mathbf{W}_{l_B}^{(B)}, \mathbf{b}_{l_B}^{(B)}\}_{l_B=1}^{L_B}, \{\mathbf{W}_{l_\eta}^{(\eta)}, \mathbf{b}_{l_\eta}^{(\eta)}\}_{l_\eta=1}^{L_\eta}\}) \right), \quad (11) \end{aligned}$$

where the $p(\mathbf{y}_h(\mathbf{s}_i)|\mathbf{x}(\mathbf{s}_i), \mathbf{z}_h, \beta_0, \boldsymbol{\beta}, \delta^2, \mathbf{F}_{L_B}^{(B)}, \mathbf{F}_{L_\eta}^{(\eta)}) = N(\mathbf{y}_h(\mathbf{s}_i)|\beta_0 + \mathbf{x}(\mathbf{s}_i)^\top \boldsymbol{\beta} + \mathbf{f}_{i, L_\eta}^{(\eta)\top} \mathbf{f}_{h, L_B}^{(B)}, \delta^2)$. Note that $\mathbf{F}_{L_\eta}^{(\eta)}$ and $\mathbf{F}_{L_B}^{(B)}$ are dependent on the weight and bias parameters $\{\mathbf{W}_{l_\eta}^{(\eta)}, \mathbf{b}_{l_\eta}^{(\eta)}\}_{l_\eta=1}^{L_\eta}$ and $\{\mathbf{W}_{l_B}^{(B)}, \mathbf{b}_{l_B}^{(B)}\}_{l_B=1}^{L_B}$, respectively. Hence, we can represent $p(\mathbf{y}_h(\mathbf{s}_i)|\mathbf{x}(\mathbf{s}_i), \mathbf{z}_h, \beta_0, \boldsymbol{\beta}, \delta^2, \mathbf{F}_{L_B}^{(B)}, \mathbf{F}_{L_\eta}^{(\eta)})$ as $p(\mathbf{y}_h(\mathbf{s}_i)|\mathbf{x}(\mathbf{s}_i), \mathbf{z}_h, \beta_0, \boldsymbol{\beta}, \delta^2, \boldsymbol{\theta})$. Since the direct maximization of (11) is challenging due to intractable integration, we can replace it with MC approximation as

$$\mathcal{L}_{\text{GP-MC}}(\beta_0, \boldsymbol{\beta}, \delta^2, \tilde{\boldsymbol{\theta}}) = \frac{1}{M} \sum_{m=1}^M \sum_{i=1}^n \sum_{h=1}^H \log p(\mathbf{y}_h(\mathbf{s}_i)|\mathbf{x}(\mathbf{s}_i), \mathbf{z}_h, \beta_0, \boldsymbol{\beta}, \delta^2, \boldsymbol{\theta}^{(m)}) - \text{KL} \left(q(\boldsymbol{\theta}|\tilde{\boldsymbol{\theta}}) \middle| \middle| p(\boldsymbol{\theta}) \right), \quad (12)$$

where $\boldsymbol{\theta}^{(m)} = \{\{\mathbf{W}_{l_\eta}^{(\eta)(m)}, \mathbf{b}_{l_\eta}^{(\eta)(m)}\}_{l_\eta=1}^{L_\eta}, \{\mathbf{W}_{l_B}^{(B)(m)}, \mathbf{b}_{l_B}^{(B)(m)}\}_{l_B=1}^{L_B}\}_{m=1}^M$ are MC samples from the variational distribution in (10). Note that the MC samples are generated for each stochastic gradient descent (SGD) update, and the estimates from $\mathcal{L}_{\text{GP-MC}}$ would converge to those obtained from $\mathcal{L}_{\text{GP-VI}}$ [Paisley et al., 2012, Rezende et al., 2014]. Further, assuming that $k_{l_B}^{(B)}$ and $k_{l_\eta}^{(\eta)}$ are both

large and σ in (10) is small, $\text{KL}\left(q(\boldsymbol{\theta}|\tilde{\boldsymbol{\theta}})\middle|p(\boldsymbol{\theta})\right)$ can be approximated as

$$\text{KL}\left(q(\boldsymbol{\theta}|\tilde{\boldsymbol{\theta}})\middle|p(\boldsymbol{\theta})\right) \approx \sum_{l_\eta=1}^{L_\eta} \frac{p_{l_\eta}}{2} (\|\boldsymbol{\mu}_{l_\eta}^{w(\eta)}\|) + \sum_{l_B=1}^{L_B} \frac{p_{l_B}}{2} (\|\boldsymbol{\mu}_{l_B}^{w(B)}\|) + \sum_{l_\eta=1}^{L_\eta} \frac{p_{l_\eta}}{2} (\|\boldsymbol{\mu}_{l_\eta}^{b(\eta)}\|) + \sum_{l_B=1}^{L_B} \frac{p_{l_B}}{2} (\|\boldsymbol{\mu}_{l_B}^{b(B)}\|),$$

upto a constant involving $k_{l_B}^{(B)}, k_{l_\eta}^{(\eta)}$ ($l_B = 1, \dots, L_B; l_\eta = 1, \dots, L_\eta$) and σ^2 . Here $\boldsymbol{\mu}_{l_\eta}^{w(\eta)} = (\mu_{l_\eta, k k'}^{w(\eta)} : k, k' = 1, \dots, k_{l_\eta}^{(\eta)})^T$, $\boldsymbol{\mu}_{l_B}^{w(B)} = (\mu_{l_B, k k'}^{w(B)} : k, k' = 1, \dots, k_{l_B}^{(B)})^T$, $\boldsymbol{\mu}_{l_\eta}^{b(\eta)} = (\mu_{l_\eta, k}^{b(\eta)} : k = 1, \dots, k_{l_\eta}^{(\eta)})^T$ and $\boldsymbol{\mu}_{l_B}^{b(B)} = (\mu_{l_B, k}^{b(B)} : k = 1, \dots, k_{l_B}^{(B)})^T$. By plugging $\text{KL}\left(q(\boldsymbol{\theta}|\tilde{\boldsymbol{\theta}})\middle|p(\boldsymbol{\theta})\right)$ approximation to (12), we have

$$\begin{aligned} \mathcal{L}_{\text{GP-MC}}(\beta_0, \boldsymbol{\beta}, \delta^2, \tilde{\boldsymbol{\theta}}) &\approx \frac{1}{M} \sum_{m=1}^M \sum_{i=1}^n \sum_{h=1}^H \log p(\mathbf{y}_h(\mathbf{s}_i) | \mathbf{x}(\mathbf{s}_i), \mathbf{z}_h, \beta_0, \boldsymbol{\beta}, \delta^2, \boldsymbol{\theta}^{(m)}) \\ &\quad - \sum_{l_\eta=1}^{L_\eta} \frac{p_{l_\eta}}{2} (\|\boldsymbol{\mu}_{l_\eta}^{w(\eta)}\|) - \sum_{l_B=1}^{L_B} \frac{p_{l_B}}{2} (\|\boldsymbol{\mu}_{l_B}^{w(B)}\|) - \sum_{l_\eta=1}^{L_\eta} \frac{p_{l_\eta}}{2} (\|\boldsymbol{\mu}_{l_\eta}^{b(\eta)}\|) - \sum_{l_B=1}^{L_B} \frac{p_{l_B}}{2} (\|\boldsymbol{\mu}_{l_B}^{b(B)}\|). \end{aligned} \quad (13)$$

The optimization of the approximated $\mathcal{L}_{\text{GP-MC}}$ in (13) will lead to the optimal estimates of $\beta_0, \boldsymbol{\beta}, \delta^2, \tilde{\boldsymbol{\theta}}$ as $\hat{\beta}_0, \hat{\boldsymbol{\beta}}, \hat{\delta}^2, \hat{\boldsymbol{\theta}}$, respectively. Note that, $\hat{\boldsymbol{\theta}}$ specifies the optimal variational distribution $q_{\text{opt}}(\boldsymbol{\theta}|\hat{\boldsymbol{\theta}})$ for the weight and bias parameters for all layers for the two generative models. We will use this optimal variational distribution along with the estimated $\hat{\beta}_0, \hat{\boldsymbol{\beta}}, \hat{\delta}^2$ to develop predictive inference, as described in the next section.

3.2 Predictive Distribution

One of advantages of our AI-driven surrogate model is that our method can quantify the uncertainty in predictions. Let $\mathbf{D} = \{(\mathbf{y}_h(\mathbf{s}_i), \mathbf{z}_h^T, \mathbf{x}(\mathbf{s}_i)^T) : h = 1, \dots, H; i = 1, \dots, n\}$ denotes the observed data. Suppose the goal is to predict the unobserved response y^* at location \mathbf{s}^* with the global covariate \mathbf{z}^* and local covariate $\mathbf{x}(\mathbf{s}^*)$. The predictive distribution can be constructed as

$$p(y^* | \mathbf{D}, \mathbf{s}^*, \mathbf{z}^*, \mathbf{x}(\mathbf{s}^*)) = \int \cdots \int p(y^* | \boldsymbol{\theta}, \beta_0, \boldsymbol{\beta}, \delta^2, \mathbf{s}^*, \mathbf{z}^*, \mathbf{x}(\mathbf{s}^*)) p(\boldsymbol{\theta}) d\boldsymbol{\theta} d\beta_0 d\boldsymbol{\beta} d\delta^2, \quad (14)$$

where $p(\boldsymbol{\theta}) = \prod_{l=1}^{L_B} p(\mathbf{W}_l^{(B)} | \mathbf{D}) p(\mathbf{b}_l^{(B)} | \mathbf{D}) \prod_{l=1}^{L_\eta} p(\mathbf{W}_l^{(\eta)} | \mathbf{D}) p(\mathbf{b}_l^{(\eta)} | \mathbf{D})$. Since it is challenging to compute (14) directly, we approximate it through MC dropout as

$$p(y^* | \mathbf{D}, \mathbf{s}^*, \mathbf{z}^*, \mathbf{x}(\mathbf{s}^*)) \approx \int \cdots \int p(y^* | \boldsymbol{\theta}, \hat{\beta}_0, \hat{\boldsymbol{\beta}}, \hat{\delta}^2, \mathbf{s}^*, \mathbf{z}^*, \mathbf{x}(\mathbf{s}^*)) q_{\text{opt}}(\boldsymbol{\theta}|\hat{\boldsymbol{\theta}}) d\boldsymbol{\theta}, \quad (15)$$

where $q_{opt}(\boldsymbol{\theta}|\widehat{\boldsymbol{\theta}})$ is the optimal variational distribution. With approximate posterior samples $\boldsymbol{\theta}^{(m)} = \{\{\mathbf{W}_l^{(B)(m)}, \mathbf{b}_l^{(B)(m)}\}_{l=1}^{L_B}, \{\mathbf{W}_l^{(\eta)(m)}, \mathbf{b}_l^{(\eta)(m)}\}_{l=1}^{L_\eta}\}_{m=1}^M$ drawn from $q_{opt}(\boldsymbol{\theta}|\widehat{\boldsymbol{\theta}})$, we adopt composition sampling, wherein the m th post burn-in iterate $y^{*(m)}$ is drawn from $p(y^{*(m)}|\mathbf{D}, \mathbf{s}^*, \mathbf{z}^*, \mathbf{x}(\mathbf{s}^*), \boldsymbol{\theta}^{(m)}, \widehat{\beta}_0, \widehat{\boldsymbol{\beta}}, \widehat{\delta}^2)$, given by $p(y^{*(m)}|\mathbf{D}, \mathbf{s}^*, \mathbf{z}^*, \mathbf{x}(\mathbf{s}^*), \boldsymbol{\theta}^{(m)}, \widehat{\beta}_0, \widehat{\boldsymbol{\beta}}, \widehat{\delta}^2) = N(\widehat{\beta}_0 + \mathbf{x}(\mathbf{s}^*)^T \widehat{\boldsymbol{\beta}} + \boldsymbol{\eta}^{(m)}(\mathbf{s}^*)^T \mathbf{B}(\mathbf{z}^*), \widehat{\delta}^2)$. Point prediction and 95% predictive intervals are computed from these predictive samples.

4 Empirical Study with Synthetic Data

This section evaluates the performance of DeepSurrogate alongside popular competing methods in drawing predictive inference for functional outcomes in unobserved simulations based on input variables and fine-scale covariates.

4.1 Data Generation

To simulate the data, we draw n spatial locations $\mathbf{s}_1, \dots, \mathbf{s}_n$ uniformly over the domain $\mathcal{D} = [0, 10] \times [0, 10]$. The data generation process involves $p = 5$ input variables and $q = 2$ fine-scale covariate. To mimic the real data structure, input vector \mathbf{z}_h for each simulation is generated from a multivariate normal distribution with mean zero and a covariance matrix $\boldsymbol{\Sigma}$, where the off-diagonal elements are set to a common correlation coefficient $\rho = 0.4$ and the diagonal elements are set to 1, i.e., $\mathbf{z}_1, \dots, \mathbf{z}_{H+H_0} \stackrel{i.i.d.}{\sim} N(\mathbf{0}, \boldsymbol{\Sigma})$. Similarly, the local attributes $\mathbf{x}(\mathbf{s}_1), \dots, \mathbf{x}(\mathbf{s}_n)$ are simulated independently from $N(\mathbf{0}, \mathbf{I}_q)$. For each $h = 1, \dots, H + H_0$ and $i = 1, \dots, n$, the response $y_h(\mathbf{s}_i)$ is drawn independently from $N(\beta_0^* + \mathbf{x}(\mathbf{s}_i)^T \boldsymbol{\beta}^* + \boldsymbol{\eta}^*(\mathbf{s}_i)^T \mathbf{B}(\mathbf{z}_h), \delta^{*2})$ following (1) and (2), where the noise variance δ^{*2} is set to be 1.

The true intercept β_0^* is set at 0.5, while each component of the coefficient $\boldsymbol{\beta}^*$ for fine-scale covariates is drawn from $U(-1.5, 1.5)$. The basis functions are chosen as the tensor-product of B-spline bases of order 4 with 5 knots, resulting in the number of basis functions to be $K = 5^p = 3125$. The true basis coefficient function $\eta_k(\cdot)$ is simulated from a Gaussian process with mean 0 and exponential covariance kernel, characterized by the spatial variance α_k^{*2} and spatial scale parameter l_k^* , such that $\text{Cov}(\eta_k(\mathbf{s}_i), \eta_k(\mathbf{s}_j)) = \alpha_k^{*2} \exp(-\|\mathbf{s}_i - \mathbf{s}_j\|/l_k^*)$.

Out of $H + H_0$ simulations, we randomly choose H simulations for model fitting, and the remaining H_0 simulations are used for testing the predictive performance of DeepSurrogate and its competitors. We consider a few different scenarios by varying the spatial variance parameter

α_k^* , spatial scale parameter l_k^* , sample size n and the number of fitted simulations H , as discussed below.

- **Scenario 1:** $n = 600$, $H = 100$, $H_0 = 20$, α_k^{*2} are drawn uniformly between $[5, 10]$, and l_k^* is drawn uniformly between $[4, 8]$, for $k = 1, \dots, K$.
- **Scenario 2:** $n = 600$, $H = 100$, $H_0 = 20$, α_k^{*2} are drawn uniformly between $[0.5, 1]$, and l_k^* is drawn uniformly between $[4, 8]$, for $k = 1, \dots, K$.
- **Scenario 3:** $n = 600$, $H = 100$, $H_0 = 20$, α_k^{*2} are drawn uniformly between $[0.5, 1]$, and l_k^* is drawn uniformly between $[0.5, 1]$, for $k = 1, \dots, K$.
- **Scenario 4:** $n = 6000$, $H = 20$, $H_0 = 20$, α_k^{*2} are drawn uniformly between $[5, 10]$, and l_k^* is drawn uniformly between $[4, 8]$, for $k = 1, \dots, K$.
- **Scenario 5:** $n = 6000$, $H = 10$, $H_0 = 20$, α_k^{*2} are drawn uniformly between $[5, 10]$, and l_k^* is drawn uniformly between $[4, 8]$, for $k = 1, \dots, K$.

Note that scenarios with higher values of α_k^* correspond to greater spatial variance, which in turn implies a higher signal-to-noise ratio (SNR) in the data. Similarly, larger values of l_k^* indicate stronger spatial dependence. We also vary the sample size n per simulation, as deep learning methods are typically data-intensive, making it important to evaluate how DeepSurrogate performs under different data availability conditions. Additionally, since a key objective of this study is to develop surrogates for expensive simulators, we evaluate performance by varying the number of fitted simulations H .

4.2 Competitors and Metric of Comparison

We implement our approach in `TensorFlow`, an open-source platform for machine learning. The computation times reported here were obtained using 8-core AMD Radeon Pro 5500 XT processors. For all simulations, we compare the proposed DeepSurrogate with function-on-scalar regression (FOSR) [Reiss et al., 2010], Bayesian adaptive smoothing spline (BASS) [Francom and Sansó, 2020] and computationally efficient alternatives for Gaussian process regression by VecchiaGP [Katzfuss and Guinness, 2021]. Both VecchiaGP and BassPCA are state-of-the-art in the surrogate literature and are widely used in national laboratories. On the other hand, FOSR is a popular method used in the functional data analysis and is computed using the `refund` package in R.

DeepSurrogate BassPCA FOSR VecchiaGP

Scenario 1	Prediction	RMSPE	2.0447	2.0241	2.4109	2.0661
	Time (min)		4.7651	0.3595	0.0356	0.4922
Scenario 2	Prediction	RMSPE	1.9960	2.0064	2.0119	2.0654
	Time (min)		4.6387	0.6263	0.0358	0.5156
Scenario 3	Prediction	RMSPE	2.0288	2.0039	2.0517	2.0656
	Time (min)		4.2577	0.6431	0.0447	0.6303
Scenario 4	Prediction	RMSPE	2.1439	2.5339	2.6022	2.1792
	Time (min)		3.0667	0.6792	0.0993	1.1322
Scenario 5	Prediction	RMSPE	2.2106	5.3651	2.9741	2.2623
	Time (min)		1.5025	0.3894	0.0335	0.3193

Table 1: Predictive point estimates for DeepSurrogate and competing methods (BassPCA, FOSR, and VecchiaGP) across five simulation scenarios are presented. For each method, root mean squared prediction error (RMSPE) and computing time (in minutes) are reported. The best performing model in terms of point prediction has been boldfaced under each scenario.

The point prediction accuracy of the competitors is evaluated using mean squared prediction error (MSPE), which measures the discrepancy between the true and the predicted responses $\sum_{h=H+1}^{H+H_0} \sum_{i=1}^n (y_h(\mathbf{s}_i) - \hat{y}_h(\mathbf{s}_i))^2 / (nH_0)$, where $\hat{y}_h(\mathbf{s}_i)$ denotes the point prediction of $y_h(\mathbf{s}_i)$, which is taken to be the posterior mean for Bayesian competitors. The predictive uncertainty is determined with the coverage probability and interval length for 95% predictive intervals (PIs) for all the competing methods over H_0 out of sample simulations.

4.3 Results

Table 1 compares the point estimation performance of competing methods. All models are well-equipped to handle functional data characteristics, demonstrating strong performance in Scenarios 1-3, where ample functional observations are available. Their accuracy remains robust regardless of variations in spatial correlation or spatial variance. However, when simulations are limited (Scenarios 4 and 5), DeepSurrogate and VecchiaGP maintain superior predictive accuracy by effectively leveraging spatial associations to estimate spatially varying relationships between inputs and outcomes, even with fewer data points. In contrast, BassPCA and FOSR rely on basis function expansions to represent functional responses. With limited functional samples, their regression parameter estimates become unstable, as the number of model parameters can vastly exceed the available data. This leads to weaker point prediction performance compared to DeepSurrogate and VecchiaGP. All methods demonstrate computational efficiency, with DeepSurrogate completing full

predictive inference for 20 simulations, each containing 6000 observations, in under 4 minutes.

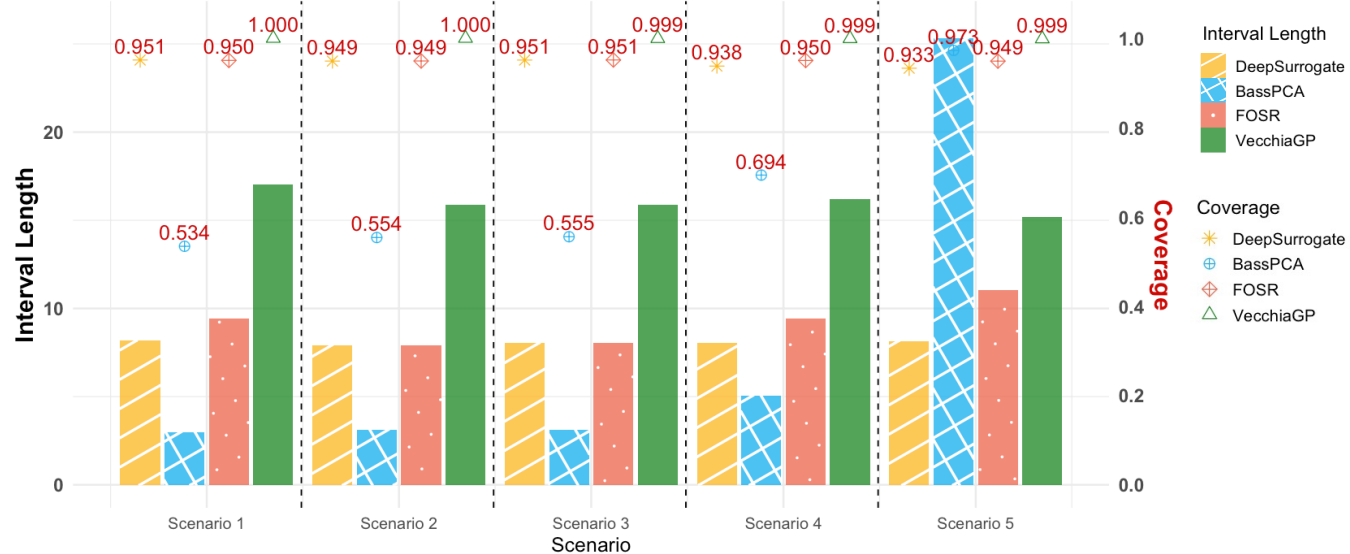


Figure 2: Comparison of predictive inference across competing models in different cases. The figure presents the interval length using a bar plot with their corresponding coverage probabilities (in red) overlaid for each scenario.

According to Figure 2, across all scenarios, DeepSurrogate consistently achieves approximately nominal coverage with well-calibrated predictive intervals. In Scenarios 1-3, where a larger number of simulations are available, BassPCA exhibits under-coverage with narrower intervals. However, as the number of simulations decreases, its estimation becomes less stable, leading to increased variability. In fact, in Scenario 5 ($H = 10$), BassPCA shows over-coverage, producing predictive intervals three times wider than those of DeepSurrogate. VecchiaGP consistently over-covers across all scenarios, with predictive intervals twice as wide as those of DeepSurrogate. FOSR performs comparably to DeepSurrogate in Scenarios 1-3 with ample simulations. As the number of simulations declines, it maintains near-nominal coverage but at the cost of wider intervals. Overall, DeepSurrogate strikes a balance between coverage accuracy and predictive interval width, outperforming competitors in scenarios with limited simulations.

4.4 Empirical Studies Under Mis-specified Data Generation Model

The empirical results in Sections 4.1–4.3 were based on the assumption that the true data-generating process follows the basis expansion model specified in (2) to induce non-linear effects of the input vectors. To evaluate the importance of this assumption, we assess the performance of

DeepSurrogate and its competitors under model misspecification. Specifically, we simulate the input attributes and fine-scale covariates as described in Section 4.1, but generate the function $f_{\mathbf{s}}(\mathbf{z}_h)$ from a Gaussian process with zero mean and an exponential covariance kernel. This kernel is defined by a spatial variance parameter α^{*2} and spatial scale parameter l^* , such that $Cov(f_{\mathbf{s}_i}(\mathbf{z}_h), f_{\mathbf{s}_j}(\mathbf{z}_{h'})) = \alpha^{*2} \exp(-\sqrt{\|\mathbf{s}_i - \mathbf{s}_j\|^2 + \|\mathbf{z}_h - \mathbf{z}_{h'}\|^2}/l^*)$. For each $h = 1, \dots, H + H_0$ and $i = 1, \dots, n$, the response $y_h(\mathbf{s}_i)$ is drawn independently from $N(\beta_0^* + \mathbf{x}(\mathbf{s}_i)^T \boldsymbol{\beta}^* + f_{\mathbf{s}_i}(\mathbf{z}_h), \delta^{*2})$ following the additive structure in (1). The true values of $\beta_0^*, \boldsymbol{\beta}^*, \delta^*$ are set as in Section 4.1.

We consider two simulation scenarios described below. Given that the main focus of this article is to develop surrogates for expensive simulations, we restrict ourselves to small values of H .

- **Scenario 1:** $n = 1000$, $H = 15$, $H_0 = 5$, α^{*2} are drawn uniformly between $[1, 5]$, and l^* is drawn uniformly between $[1, 5]$.
- **Scenario 2:** $n = 2000$, $H = 6$, $H_0 = 4$, α^{*2} are drawn uniformly between $[1, 5]$, and l^* is drawn uniformly between $[1, 5]$.

	DeepSurrogate	BassPCA	FOSR	VecchiaGP
Scenario 1	2.3242	2.1662	3.0531	2.3430
Scenario 2	2.3186	4.5696	2.8357	2.3623

Table 2: Predictive point estimates for DeepSurrogate and competing methods (BassPCA, FOSR, and VecchiaGP) across the two simulation scenarios under model mis-specification are presented. For each method, root mean squared prediction error (RMSPE) is reported. The best performing model under each scenario is boldfaced.

The results from Scenarios 1 and 2 under model misspecification largely mirror the conclusions drawn from the earlier simulations assuming correct model specification (refer to Table 2). In Scenario 1, with a sample size $n = 1000$ and number of simulations set to $H = 15$, DeepSurrogate and VecchiaGP achieve comparable point prediction accuracy, while BassPCA shows a slight advantage. In contrast, when the sample size increases to $n = 2000$ and the number of simulations is reduced to $H = 6$, the primary setting of interest in this study, DeepSurrogate delivers the most accurate point predictions, with VecchiaGP performing competitively and BassPCA showing notably poorer performance. In both scenarios, DeepSurrogate consistently and substantially outperforms FOSR.

As shown in Figure 3, in both scenarios, DeepSurrogate provides predictive intervals that are

well-calibrated and achieve coverage probabilities close to the nominal level. FOSR also attains near-nominal coverage but produces noticeably wider credible intervals compared to DeepSurrogate. BassPCA exhibits substantial under-coverage in both scenarios, while VecchiaGP achieves nearly the full coverage with two-to-three-fold increase in predictive interval length compared to DeepSurrogate.

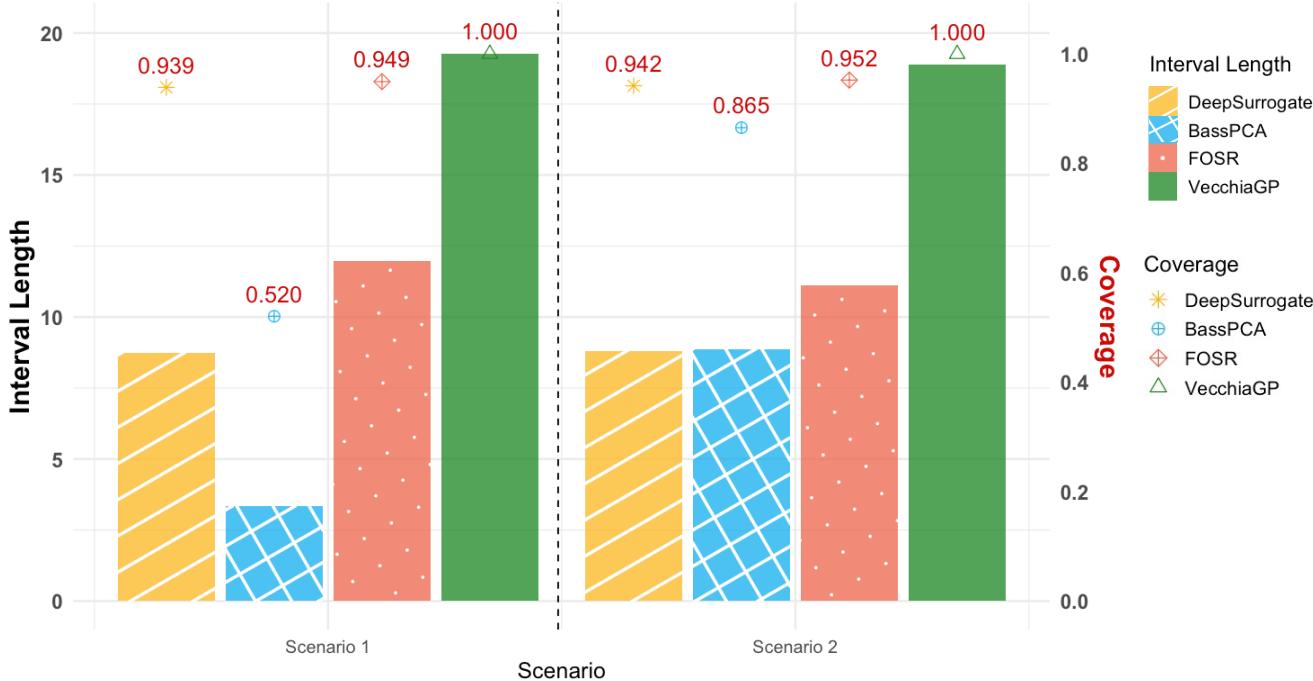


Figure 3: Comparison of predictive inference across competing models in different cases. The figure presents the interval length using a bar plot with their corresponding coverage probabilities (in red) overlaid for each scenario.

5 SLOSH Emulator Data Analysis

This section presents the application of our Artificially Intelligent Functional Surrogate Model, referred to as DeepSurrogate, to analyze storm surge simulation data alongside competing models. Storm surge models play a crucial role in emergency response, planning, and research by simulating floodwater depths caused by hurricanes. Among these, the Sea, Lake, and Overland Surges from Hurricanes (SLOSH) simulator [Jelesnianski, 1992], developed by the National Weather Service, is one of the most widely used models.

Since the goal is to test efficacy of DeepSurrogate under limited simulations for its potential usage in expensive simulation settings, we analyze a dataset consisting of 30 simulations generated

Predictor	Lower	Upper	Units
Heading	204.0349	384.0244	degrees
Velocity	0	40	knots
Latitude	38.32527	39.26811	degrees
Pressure	930	980	millibars
Sea level rise (2100)	-20	350	cm

Table 3: Parameters varied in SLOSH simulations.

using the SLOSH simulator, each representing a distinct hypothetical storm scenario. These storms are defined by unique combinations of five input parameters. Four parameters describe the hurricane at landfall: the heading of the eye, the velocity of the eye, the latitude of the eye, and the minimum air pressure. The fifth parameter, projected sea level rise for the year 2100, introduces an element of uncertainty into the system.

The parameter ranges, outlined in Table 3, reflect realistic variations and were used to generate the simulation scenarios. This ensemble serves as a testbed for developing functional surrogates that enable efficient analysis and prediction in the context of computationally expensive storm surge simulations. The primary focus of this study is assessing storm surge-induced damage to electrical power stations. Since most power stations are located inland and remain unaffected, we specifically analyze functional data consisting of simulated storm surge heights at $n = 49,719$ spatial locations to predict hurricane-induced flooding in the southern tip of New Jersey (see Figure 4) for each simulation. A map illustrating the output from a single SLOSH simulation over the spatial domain of interest is provided in Figure 4. Additionally, elevation data is available for each spatial location of the electrical power stations. Given the critical role of this covariate in assessing maximum flood heights at specific locations, we incorporate elevation as a *fine-scale covariate* in our analysis to enhance predictive accuracy.

To evaluate the out-of-sample predictive performance of the competitors, we utilize 10 simulation datasets for model fitting, and 10 simulations generated by the SLOSH simulator for testing. Given that each simulation contains data for 49,719 locations, this yields predictive inference on $n_{\text{test}} = 497,190$ out-of-sample observations.

Mis-classification error for power stations. Power stations in the Delaware Bay region are typically designed to withstand flooding up to four feet, beyond which severe damage becomes

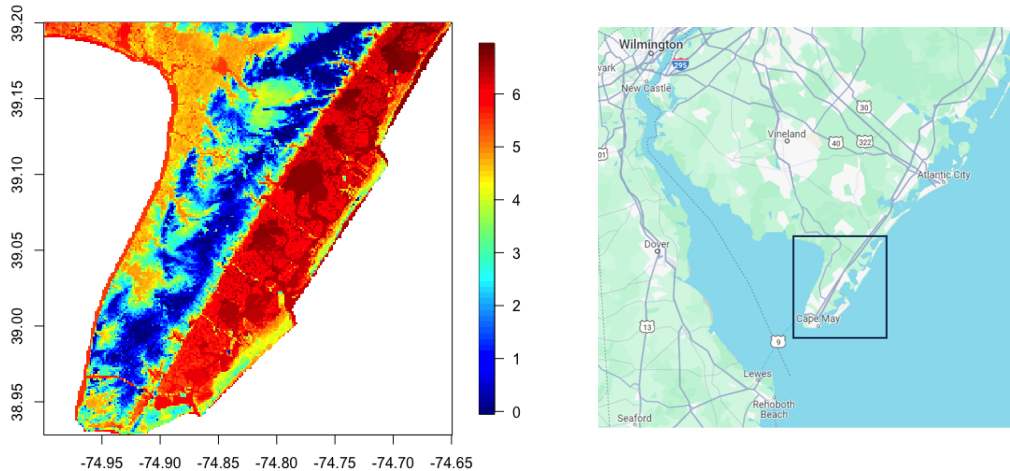


Figure 4: Output from one SLOSH model run, side-by-side with the location of the peninsula in Google Maps. Here, x and y axes represent longitude and latitude, respectively.

inevitable. Therefore, we also evaluate the emulator’s ability to accurately predict whether a storm surge exceeds this critical threshold. Specifically, we report the percentage of misclassification, where a misclassification occurs when a true storm surge height above four feet is incorrectly predicted as below four feet, or vice versa. This predictive capability is crucial for informed decision-making, enabling timely interventions such as preemptively shutting down power stations in preparation for an approaching storm.

5.1 Results

The actual and predicted storm surge for a randomly selected test storm, shown in Figure 5, illustrate that DeepSurrogate effectively captures local spatial storm surge patterns.

Table 4 indicates that VecchiaGP achieves the lowest RMSPE and misclassification rate, suggesting superior point prediction performance, with DeepSurrogate being highly competitive. However, in terms of uncertainty quantification, DeepSurrogate outperforms VecchiaGP, providing well-calibrated 95% predictive intervals with approximately nominal coverage. In contrast, VecchiaGP exhibits under-coverage due to its narrower intervals. Thus, while VecchiaGP excels in mean prediction, DeepSurrogate offers a better balance of accuracy and predictive uncertainty.

Consistent with simulation results, BassPCA struggles with fewer simulations, yielding higher RMSPE and misclassification rates compared to both DeepSurrogate and VecchiaGP. FOSR performs the worst in point prediction, while both FOSR and BassPCA produce excessively wide

predictive intervals with 100% coverage, indicating overly conservative uncertainty estimates.

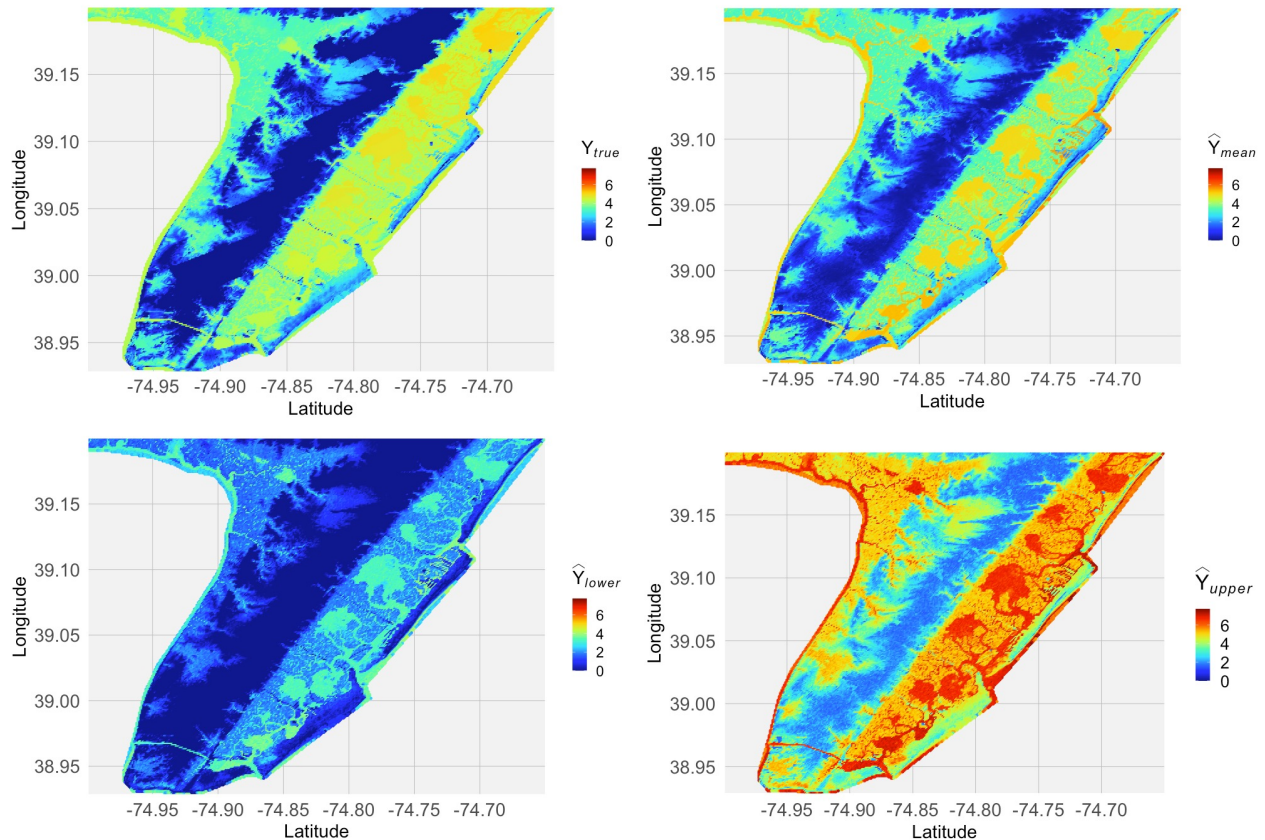


Figure 5: The left-upper figure and the right-upper figure show the actual storm surge and the estimated storm surge in a randomly selected out-of-sample simulation. The left-bottom and the right-bottom figures provide 2.5% and 97.5% predictive interval limits.

	RMSPE	Error %	Coverage	Length	Comp. time (in min.)
BassPCA	1.81	0.18	1.00	11.51	0.41
VecchiaGP	0.78	0.11	0.80	2.01	2.36
FOSR	2.14	0.47	1.00	8.28	0.37
DeepSurrogate	0.90	0.13	0.94	3.44	8.03

Table 4: The table summarizes the predictive performance of DeepSurrogate and its competitors—VecchiaGP, BassPCA, and FOSR—across 10 out-of-sample simulations. It reports the root mean squared prediction error (RMSPE), misclassification error rate for power stations (Error%), coverage of 95% predictive intervals, average length of 95% predictive intervals, and computation time (in minutes) for all methods.

6 Conclusion and Future Work

This article introduces DeepSurrogate, an explainable AI framework for modeling functional surrogates with vector-valued inputs in physics-driven simulations. The framework captures spatial dependencies in the functional output, models the relationship between functional outputs and inputs, and integrates Monte Carlo (MC) dropout for uncertainty quantification within a DNN framework, enhancing explainability of DNN-based framework. When simulations are computationally expensive and limited, DeepSurrogate provides accurate predictions with well-calibrated uncertainty estimates. It is competitive in point prediction with popular alternatives while offering superior uncertainty quantification. Additionally, it remains computationally efficient, delivering full predictive inference for 50,000 locations in under 10 minutes.

While our framework has been employed to develop efficient surrogates, it has important applications in statistical imaging. As a natural extension of our work, we aim to develop an AI-based generative modeling framework for image-on-image regression where input and output images are structurally misaligned. In this setting, spatial dependencies will play a crucial role in prediction; however, additional topological structures, such as network-based associations between image regions, may also significantly influence the modeling process. In an ongoing work, we are exploring methodologies that integrate both spatial and network-driven dependencies in images.

References

- R. J. Andros, R. Guhaniyogi, D. Francom, and D. Pasqualini. Robust distributed learning of functional data from simulators through data sketching, 2024. URL <https://arxiv.org/abs/2406.18751>.
- N. Bliznyuk, D. Ruppert, C. Shoemaker, R. Regis, S. Wild, and P. Mugunthan. Bayesian calibration and uncertainty analysis for computationally expensive models using optimization and radial basis function approximation. *Journal of Computational and Graphical Statistics*, 17(2):270–294, 2008.
- R. Borge, V. Alexandrov, J. J. Del Vas, J. Lumbreras, and E. Rodríguez. A comprehensive sensitivity analysis of the wrf model for air quality applications over the iberian peninsula. *Atmospheric Environment*, 42(37):8560–8574, 2008.

- H. A. Chipman, E. I. George, and R. E. McCulloch. Bart: Bayesian additive regression trees. *The Annals of Applied Statistics*, 4(1):266 – 298, 2010. doi: 10.1214/09-AOAS285. URL <https://doi.org/10.1214/09-AOAS285>.
- N. Cressie. *Statistics for spatial data*. John Wiley & Sons, 2015.
- N. Cressie and G. Johannesson. Fixed rank kriging for very large spatial data sets. *Journal of the Royal Statistical Society Series B: Statistical Methodology*, 70(1):209–226, 2008.
- A. Damianou and N. D. Lawrence. Deep gaussian processes. In *Artificial intelligence and statistics*, pages 207–215. PMLR, 2013.
- A. H. El-Shaarawi and W. W. Piegorsch. *Encyclopedia of environmetrics*, volume 1. John Wiley & Sons, 2002.
- D. Francom and B. Sansó. BASS: An R package for fitting and performing sensitivity analysis of Bayesian adaptive spline surfaces. *Journal of Statistical Software*, 94(LA-UR-20-23587), 2020.
- Y. Gal and Z. Ghahramani. Dropout as a bayesian approximation: Representing model uncertainty in deep learning. In *international conference on machine learning*, pages 1050–1059. PMLR, 2016.
- J. Goldsmith, J. Bobb, C. M. Crainiceanu, B. Caffo, and D. Reich. Penalized functional regression. *Journal of computational and graphical statistics*, 20(4):830–851, 2011.
- J. Goldsmith, V. Zipunnikov, and J. Schrack. Generalized multilevel function-on-scalar regression and principal component analysis. *Biometrics*, 71(2):344–353, 2015.
- F. A. Gomes and T. A. Senne. An algorithm for the topology optimization of geometrically nonlinear structures. *International Journal for Numerical Methods in Engineering*, 99(6):391–409, 2014.
- R. B. Gramacy. *Surrogates: Gaussian process modeling, design, and optimization for the applied sciences*. Chapman and Hall/CRC, 2020.
- R. B. Gramacy and D. W. Apley. Local gaussian process approximation for large computer experiments. *Journal of Computational and Graphical Statistics*, 24(2):561–578, 2015.
- R. Guhaniyogi and B. Sanso. Large multi-scale spatial modeling using tree shrinkage priors. *Statistica Sinica*, 30(4):2023–2050, 2020.

- R. Guhaniyogi, C. Li, T. D. Savitsky, and S. Srivastava. Distributed bayesian varying coefficient modeling using a gaussian process prior. *The Journal of Machine Learning Research*, 23(1):3642–3700, 2022.
- R. Guhaniyogi, C. Li, T. Savitsky, and S. Srivastava. Distributed bayesian inference in massive spatial data. *Statistical science*, 38(2):262–284, 2023.
- R. Guhaniyogi, L. Baracaldo, and S. Banerjee. Bayesian data sketching for varying coefficient regression models. 2024.
- D. Higdon, M. Kennedy, J. C. Cavendish, J. A. Cafeo, and R. D. Ryne. Combining field data and computer simulations for calibration and prediction. *SIAM Journal on Scientific Computing*, 26(2):448–466, 2004.
- C. P. Jelesnianski. *SLOSH: Sea, lake, and overland surges from hurricanes*, volume 48. US Department of Commerce, National Oceanic and Atmospheric Administration . . . , 1992.
- M. Katzfuss and J. Guinness. A general framework for vecchia approximations of gaussian processes. *Statistical Science*, 36(1):124–141, 2021.
- F. Lindgren, H. Rue, and J. Lindström. An explicit link between gaussian fields and gaussian markov random fields: the stochastic partial differential equation approach. *Journal of the Royal Statistical Society Series B: Statistical Methodology*, 73(4):423–498, 2011.
- A. Marrel, B. Iooss, M. Jullien, B. Laurent, and E. Volkova. Global sensitivity analysis for models with spatially dependent outputs. *Environmetrics*, 22(3):383–397, 2011.
- J. S. Morris. Functional regression. *Annual Review of Statistics and Its Application*, 2(1):321–359, 2015.
- H. N. Najm. Uncertainty quantification and polynomial chaos techniques in computational fluid dynamics. *Annual review of fluid mechanics*, 41(1):35–52, 2009.
- J. Paisley, D. Blei, and M. Jordan. Variational Bayesian inference with stochastic search, 2012.
- M. R. Petersen, X. S. Asay-Davis, A. S. Berres, Q. Chen, N. Feige, M. J. Hoffman, D. W. Jacobsen, P. W. Jones, M. E. Maltrud, S. F. Price, et al. An evaluation of the ocean and sea ice climate of

- e3sm using mpas and interannual core-ii forcing. *Journal of Advances in Modeling Earth Systems*, 11(5):1438–1458, 2019.
- A. R. Rao, Q. Wang, H. Wang, H. Khorasgani, and C. Gupta. Spatio-temporal functional neural networks. In *2020 IEEE 7th International Conference on Data Science and Advanced Analytics (DSAA)*, pages 81–89. IEEE, 2020.
- P. T. Reiss and R. T. Ogden. Functional principal component regression and functional partial least squares. *Journal of the American Statistical Association*, 102(479):984–996, 2007.
- P. T. Reiss, L. Huang, and M. Mennes. Fast function-on-scalar regression with penalized basis expansions. *The international journal of biostatistics*, 6(1), 2010.
- D. J. Rezende, S. Mohamed, and D. Wierstra. Stochastic backpropagation and approximate inference in deep generative models. In *International Conference on Machine Learning*, pages 1278–1286. PMLR, 2014.
- F. Rossi and B. Conan-Guez. Functional multi-layer perceptron: a non-linear tool for functional data analysis. *Neural networks*, 18(1):45–60, 2005.
- F. Rossi, B. Conan-Guez, and F. Fleuret. Functional data analysis with multi layer perceptrons. In *Proceedings of the 2002 International Joint Conference on Neural Networks. IJCNN’02 (Cat. No. 02CH37290)*, volume 3, pages 2843–2848. IEEE, 2002.
- H. Rue, S. Martino, and N. Chopin. Approximate bayesian inference for latent gaussian models by using integrated nested laplace approximations. *Journal of the Royal Statistical Society Series B: Statistical Methodology*, 71(2):319–392, 2009.
- T. Santner. *The design and analysis of computer experiments*, 2003.
- A. Sauer, R. B. Gramacy, and D. Higdon. Active learning for deep gaussian process surrogates. *Technometrics*, 65(1):4–18, 2023.
- F. Scheipl, A.-M. Staicu, and S. Greven. Functional additive mixed models. *Journal of Computational and Graphical Statistics*, 24(2):477–501, 2015.

- B. Thind, K. Multani, and J. Cao. Neural networks as functional classifiers. *arXiv preprint arXiv:2010.04305*, 2020.
- B. Thind, K. Multani, and J. Cao. Deep learning with functional inputs. *Journal of Computational and Graphical Statistics*, 32(1):171–180, 2023.
- B. Vidakovic. *Statistical modeling by wavelets*. John Wiley & Sons, 2009.
- H. Wang and J. Cao. Nonlinear prediction of functional time series. *Environmetrics*, 34(5):e2792, 2023.
- H. Wang and J. Cao. Functional nonlinear learning. *Journal of Computational and Graphical Statistics*, 33(1):181–191, 2024.
- Q. Wang, H. Wang, C. Gupta, A. R. Rao, and H. Khorasgani. A non-linear function-on-function model for regression with time series data. In *2020 IEEE International Conference on Big Data (Big Data)*, pages 232–239. IEEE, 2020.
- S. Wu, C. Beaulac, and J. Cao. Neural networks for scalar input and functional output. *Statistics and Computing*, 33(5):118, 2023.
- D. Xiu and G. E. Karniadakis. The wiener–askey polynomial chaos for stochastic differential equations. *SIAM journal on scientific computing*, 24(2):619–644, 2002.
- F. Yao and T. C. Lee. Penalized spline models for functional principal component analysis. *Journal of the Royal Statistical Society Series B: Statistical Methodology*, 68(1):3–25, 2006.
- J. Yao, J. Mueller, and J.-L. Wang. Deep learning for functional data analysis with adaptive basis layers. In *International Conference on Machine Learning*, pages 11898–11908. PMLR, 2021.
- H. Zhang and P. M. Dower. Max-plus based computation of nonlinear l2-gain performance bounds using a piecewise affine-quadratic basis. In *2013 European Control Conference (ECC)*, pages 2232–2237. IEEE, 2013.
- X. Zhang and J.-L. Wang. Varying-coefficient additive models for functional data. *Biometrika*, 102(1):15–32, 2015.